Research Square

Preprints are preliminary reports that have not undergone peer review.
They should not be considered conclusive, used to inform clinical practice,
or referenced by the media as validated information.

The effectiveness of Nano clinoptilolite for the removal of two pharmaceutical drugs from water: An eco-friendly water remediation approach

Shorouk Goda
Beni-Suef University
Ahmed Hassan
Beni-Suef University
Tabbi Wilberforce
king's college London
Nabila shehata
nabila.shehata@psas.bsu.edu.eg

Beni-Suef University

Research Article

Keywords: Nanoclinoptilolite, Adsorption, Zeolite, Tetracycline, wastewater treatment, Emerging pollutants, Mebeverine hydrochloride

Posted Date: November 5th, 2026

DOI: https://doi.org/10.21203/rs.3.rs-11412141/v1

License: This work is licensed under a Creative Commons Attribution 4.0 International License.
Read Full License

Additional Declarations: No competing interests reported.

Abstract

Pharmaceutical residues, such as Mebeverine (MEB) and Tetracycline (TC), are difficult to remove from aquatic habitats because they are resistant to typical wastewater treatment techniques. This research studies the efficiency of synthesized nano-clinoptilolite (NCpt) as an eco-friendly, affordable, powerful adsorbent for the removal of these contaminants. Characterization results show that the initiated adsorbent has a clinoptilolite structure with an average crystallite size of 11.1 nm. The specific surface area based on BET calculation was 34.15 m^2/g, with findings indicating a pore-mouth blocking mechanism; as adsorption occurred predominantly on external active sites while the total pore volume remained relatively stable (0.16 cm^3/g). The adsorption batch experiments determined a maximum adsorption capacity of 22.19 mg/g for TC and 76.9 mg/g for MEB. The kinetic model's data showed excellent fits with the Pseudo-Second Order (PSO) and Mixed 1,2-Order (MFSO) models (R^2 0.95–0.99), suggesting a synergistic mechanism between chemisorption and physisorption. Moreover, isotherm analysis data highlighted the heterogeneity of the NCpt surface, with Toth (R^2 = 0.971) and Redlich-Peterson (R^2 = 0.971) models providing the best description for MEB, and Langmuir-Freundlich (R^2 = 0.966) and Sips (R^2 = 0.955) models for TC. Moreover, the reusability test of NCpt was successfully validated through multiple cycles using green tea and ethanol as desorption solvents. The results showed that NCpt established as a sustainable and highly efficient material for environmental remediation in treating pharmaceutical-contaminated wastewater.

1. Introduction

Pharmaceuticals and personal care products (PPCPs) are progressively classified as crucial emerging micropollutants as a result of their global presence and the ecological challenges they create [1]. These emerging compounds, which include antimycotics, anti-inflammatories, surfactants and UV-filters, are permanently put into grey water (GW) and municipal streams through daily human activities [2]. Residues of pharmaceutical are directed into aquatic ecosystems through a centralized wastewater treatment plants (WWTPs), which act as the main entry point, once the residues enter the wastewater stream [3]. A variety complicated mixtures of residues are introduced to these facilities from different sources, such as household waste, industrial discharges, and—most importantly—hospital effluents (HWW), which include high quantities of specialist medications.

Recent studies have shown that hospital effluents can contain pharmaceutical concentrations as high as 58,520 ng L^{-1} for certain analgesics and more than 7,000 ng L^{-1} for opioids after treatment. This points out a significant research/technical gap, since conventional WWTPs are reported to have variable removal efficiencies, with some even showing negative removal efficiency values, reflecting that these pollutants are not only poorly removed but perhaps even more concentrated during the process [4]. Biodegradability and chemical stability are poor for many drugs and their metabolites, and only partially eliminated. They are either released directly into the receiving water bodies, or they remain in the sewage sludge, thereby creating a continuous cycle of contamination that poses a risk to public health [5].

Among these, Mebeverine Hydrochloride (MEB) and Tetracycline (TC) are two pharmaceutical residues of particular concern. Mebeverine hydrochloride is a potent muscarinic antispasmodic, mainly used in the treatment of diseases of the genitourinary and vascular systems and gastrointestinal disorders such as irritable bowel syndrome (IBS) (Daniluk et al., 2022). Pharmacologically, MEB is very soluble in water and has a relatively short biological half-life, requiring frequent administration in high therapeutic doses. High consumption rate and chemical stability lead to a continuous and considerable discharge of MEB into municipal wastewater streams [6]. MEB was specifically chosen as a model pollutant in this study due to its high-risk characterization ratio (RCR) and increasing reports of its frequency worldwide. Importantly, MEB has been identified as a high-priority contaminant with RCR values exceeding 1 in major regional cities (Hussein Al-Timimi et al., 2023). Moreover, the molecular design of MEB, often formulated with extended-release polymers to prevent 'drug dumping', contributes to its persistence in the environment, as these residues are not readily degraded or eliminated by conventional wastewater treatment processes. Despite its extensive use in clinical settings for decades, there is a severe lack of ecotoxicological data regarding its long-term effects on aquatic ecosystems (Tao et al., 2025) (Zhang et al., 2023).

Moreover, TC antibiotics are one of the main classes of antibiotics used in veterinary care, human treatment, and agriculture. Tetracycline is detected widely in surface water, groundwater, drinking water, and wastewater [7]. Typical concentration range in natural waters is 0–20 ng/L in Europe, Henan Province (China) drinking water showed TCs at ND–3.23 ng/L [8], and Tigris River samples contained oxytetracycline (0.037–1.756 ng L^{-1}), TC (0.004–0.014 ng L^{-1}) and chlortetracycline (0.015–0.097 ng L^{-1}) [9]. Tetracyclines are given more attention than other antibiotics because they have major negative effects on fish physiology & histopathology [10], TCs more toxic to algae than fish/daphnia; disrupt microbial communities, and induce antibiotic resistance genes (ARGs) [11]. High accumulation in soil and manure runoff increases loading to water bodies; causes microbial community shifts [12], and it is worth noting that photolysis and hydrolysis produce multiple metabolites that retain ecotoxicity even when parent TC degrades [13]. Following treatment, almost 70% of TC antibiotics are eliminated and released into the environment in active form through animal and human urine and feces [7]. Their considerable endurance in the aquatic environment is a result of their low volatility and extremely hydrophilic nature. A critical necessity of wastewater recycling and safe reuse is underscored in 2015 by United Nations Sustainable Development Goal 6 (UN SDG 6) to ensure universal access to water resources. In the face of global water scarcity, the irrigation of agricultural lands with reclaimed wastewater has become an essential strategy. However, the intersection of these two needs advanced healthcare and water sustainability presents a complex challenge: ensuring that recycled water is free from pharmaceutical residues that sustain human health but threaten aquatic ecosystems [14] [15]. Consequently, developing efficient remediation strategies, such as adsorption, has become a topic of high priority to alleviate the potential environmental dangers related to MEB and TC pollutions. Hence, scavenge of these drug residues from water is important.

Clays are natural adsorbents that exist in high abundance in nature and categorized as high-abundance adsorbents with exceptional physicochemical properties [16]. Their unique ability to intercalate pharmaceutical compounds within layered or porous structures has positioned them as leading candidates for environmental remediation and drug delivery [17]. Among the used clays, NCpt is one of the most available natural minerals that have been utilized in waste and toxins disposal from aqueous medium. Over the past decades, NCpt has attracted considerable attention as an economically and environmentally friendly option; their use has expanded from traditional petrochemical refineries to the catalytic degradation of emerging pollutants and the synthesis of fine chemicals [18]. Structurally, NCpt are defined as crystalline, hydrated aluminosilicates with a robust three-dimensional open framework. This framework is characterized by the general common formula: $M_{x/n}\,[Al_xSi_yO_{2(x+y)}]\cdot zH_2O$, where M refers to an alkali or alkaline earth metal cation, and z denotes the water of crystallization. According to Tsintskaladze et al. (2026), clinoptilolite stands out among the many zeolitic frameworks because of its exceptional ion-exchange capacity and great thermal stability. This mineral has been further optimized by recent developments in nanotechnology; specifically, the synthesis of NCpt demonstrates improved diffusivity and a larger density of active sites. This development is crucial for the efficient sequestration of complex emerging micropollutants like TC and MEB, which are frequently not eliminated by the treatment systems [19].

Therefore, the purpose of this work is to critically analyze and investigate the potential of NCpt as a high-performance, sustainable adsorbent to address the growing problem of pharmaceutical water pollution focusing on two notable recently discovered pollutants, the broad-spectrum antibiotic TC and the antispasmodic medication MEB. The adsorption efficiency, kinetic mechanisms, and physicochemical interactions of the NCpt framework have been evaluated. By using a batch of adsorption experiments, such as contact time, initial concentrations, and adsorbent dosage, and analyzing their effect. The novelty of this research is to prepare a cost-effective and scalable strategy based on natural resources to help in the removal process of complex pharmaceutical residues from wastewater supporting the global transition toward safe and resumed water reuse strategies.

2. Materials and Methods

2.1 Material

Mebeverine hydrochloride ($C_{25}H_{35}NO_5$) was supplied by Chemipharma, Egypt (Scheme 1a). Tetracycline hydrochloride with a molecular weight ~ 480.90 g/mol and formula [$C_{22}H_{25}ClN_2O_8$] was obtained from CID Pharm, Egypt (Scheme 1b). Absolute ethanol (100%) was supplied by Sigma-Aldrich. EMSURE (Germany) provided sodium hydroxide (NaOH), while SDFCL (India) supplied hydrochloric acid (HCl, 35.4% AR grade).

(b)

Scheme 1: The chemical structure of TC (a) and MEB (b)

Commercial clinoptilolite zeolite [$(Na_2, K_2 Ca)Al_6Si_{30}O_{72}{\cdot}21H_2O$] cleaned with water then dried for 48 h at 100°C. After that the ball milling used for 24 h at 900 rpm where the ball-to-powder ratio was 50:1 to minimize its particle size (Scheme 2).

2.2 Instrumentation

UV/Vis spectrometer model T80 (China), was used for determination of absorbance spectra. AD1030 pH meter (Romania) integrated with a reference electrode has been used to measure the solutions pHs. Rotor shaker (SCILOGEX, SK-O330-Pro) integrated with a timer has been used for batch arrays. PLC-036 centrifuge (Taiwan) has been used for sample separation purposes. Hot plate and magnetic stirrers (MS-330HS, Korea) are used to adjust the solution temperature and mixing.

2.3 Characterization of the materials

The materials characterization was accomplished before and after adsorption utilizing various techniques; X-ray diffractometer (Panalytical Empyrean, 202964, Sweden) equipped with Cu-Kα radiation worked at a current of 35 mA and 40 kV voltage with a 1.54060 Å wavelength in the diffraction angle ranging from 5° to 80° is utilized to explore the structural composition and crystallinity of the materials. To elucidate the structure and surface characteristics of the developed material, FE-SEM (Zeiss - Sigma 500 VP - Germany) was used. FT-IR (model, Bruker Vertex 70, Germany) was utilized to investigate the variety of the bonds of the materials within a wave number of 400–4000 cm^{-1} range. Hydrodynamic particle size was calculated by Nano-Zetasizer supplied from Malvern Instruments Ltd (UK). The specific surface area, pore size distribution, and pore volume of the formulated specimens were estimated from the N_2 adsorption-desorption isotherm based on TriStar II 3020 Version 3.02 (Quantachrome Instrument, Italy).

2.4 Batch adsorption arrays

Experiments were conducted in the pH range of 2–10 to investigate the impact of pH. The solutions' pH was changed by adding 1 M NaOH or HCl. The impact of dose onto the adsorption performance has been accessed by the preparation of 20 mL (MEB or TC) solution in contact with 0.01, 0.03, 0.07, or 0.1g, then left them at shaker for 12 h. For the initial concentration (C_o) arrays, 20 mL of TC or MEB solutions with specific concentrations varying from 5 to 400 mgL^{-1} were added to the optimum dose of NCpt at optimum pH and were mixed using a shaker for 12 h to make sure it reaches the equilibrium. After separation by centrifuge, the supernatant was maintained for measuring the absorbance using UV–Vis spectroscopy at wavelength 275 nm. The effect of retention time on the adsorption performance of NCpt was studied at two different concentrations of both drugs (TC and MEB) using 250 mL water, 0.12 g from NCpt was added then the impact of time was measured after 5, 10, 15, 30, 60, 120, 180, 240, 300 and 1440 min. Each experiment has been triplicated to ensure reproducibility.

2.5 Calculations

The amount of adsorption at equilibrium, q_e (mgg^{-1}), and the percentage of drug removal were calculated according to Eqs. 1 and 2, respectively.

$$q_e = \frac{(C_o - C_e) * v}{w}$$

1

$$R\% = \frac{(C_o - C_e) * 100}{C} \quad (2)$$

Where *v* is the volume of the drug solution (L), C_e (mgL^{-1}) is the liquid-phase conc. of TC and MEB at equilibrium, respectively, and *w* is the mass of dry adsorbent used (g).

3. Results and discussion

3.1 Process optimization

3.1.1 Preliminary results

The selectivity of NCpt toward antibiotics and different pharmaceuticals of emerging concern has been investigated. Hence, the adsorptivity of NCpt towards Nanaxozid (Nitazoxanide), Suprax (Cefixime), Clindam (Clindamycin), Epimole (Paracetamol), Caffeine (Caffeine), Dalacin (Clindamycin), Antinal (Nifuroxazide), Amoxi (Amoxicillin), Ampicillin (Ampicillin), Dantrelax (Dantrolene), After Meals (Diastase, Papain, Simethicone), Cefolcar (Cefotaxime), E-Mox (Amoxicillin), Tetracycline (Tetracycline) and Coleverin SR (Mebeverine HCl) have been investigated. The preliminary results show that NCpt shows good selectivity towards both Tetracycline and Coleverin SR (Mebeverine HCl). Accordingly, the subsequent arrays have been conducted on both drugs.

1.1.2 pH effect

As pH rises, Figure (1a) shows a steady increase in adsorption capacity, beginning at 13.26 mg/g (R% = 13.0%) at pH 1.5 and reaching a maximum of 25.3 mg/g (R% = 26.3%) at pH 9. This behavior is explained by the fact that MEB is a strong antispasmodic medication with a tertiary amine structure that makes it a cationic pharmaceutical that is sensitive to pH. Its pKa value is roughly 7.8–8.2, which indicates that the medication is mostly present in its protonated cationic form (MEB^+) in the pH range of our tests (1.5–7.0). In highly acidic conditions (pH 1.5–3.3), the adsorption efficiency is relatively low [20]. This is attributed to the high concentration of hydronium ions (H^+) in the solution, which compete fiercely with the cationic MEB^+ molecules for the negatively charged active sites on the NCpt surface (Zeta potential = − 13.5 mV). As the pH increases toward 9.0, the concentration of competing H^+ ions decreases. This reduction in proton competition allows the electrostatic attraction between the negatively charged NCpt surface and the cationic MEB^+ molecules to become the dominant operative force, thereby maximizing adsorption efficiency at pH 9.0. [21]

The adsorption of TC onto NCpt exhibits a reverse behavior where the acidic media promotes the adsorption of TC onto NCpt. Figures (1b) shows that the maximum adsorption (39.26 mg/g) and R% = 27.6% occurred at pH 3.03. This because TC shows a cationic interaction in acidic media. At pH 3.03, TC is primarily in its positively charged form (TC^{+}), as the solution pH is below its first pKa (3.3) [22]. The negative zeta potential of NCpt − 13.5 mV is sufficient to initiate strong electrostatic coupling with the TC^{+} cations. The decline in removal efficiency at pH > 3.03 corresponds to the transition of TC into its zwitterionic form (TC^{0} at 3.3 ≤ pH ≤ 7.7) [23] [24]. In this state, the net charge of the molecule is zero, which weakens the long-range electrostatic attraction toward the NCpt surface, leading to a temporary decline in performance. At this pH, TC begins to carry a net negative charge and the presence of localized positive charges within the complex TC structure can still interact with the negative NCpt surface. Also, the solubility of TC is the lowest at pH 3.3–7.7 which enhances the adsorption onto NCpt. Furthermore, the 285 nm particle size suggests that intra-particle diffusion and "pore filling" become dominant, where the zeolitic framework traps the bulky TC molecules despite the shifting charges. The minimum removal % (15.43%) and adsorption capacity (21.17 mgg^{-1}) achieved pH 10.4. At this highly alkaline pH, the TC molecule is fully deprotonated and carries a strong negative charge (TC^{2-}). Simultaneously, the NCpt surface is at its most negative state [25]. The resulting strong electrostatic repulsion between the negatively charged adsorbent and the negatively charged adsorbate completely inhibits any molecular approach to the surface, rendering the adsorption process impossible. Despite the maximum adsorption capacities of MEB and TC occurred at pH 9 and 3; However, we conducted the subsequent adsorption arrays at pH values 7 and 5, respectively. This decision is based on a balanced approach between adsorption efficiency and practical feasibility. In real-world wastewater treatment, maintaining extremely low (acidic) or high (alkaline) pH levels is economically expensive and operationally corrosive. Therefore, we optimized our conditions to be as close as possible to the near-neutral range, which provides a high-performance, sustainable, and cost-effective solution for industrial application.

3.1.3 Effect of dose

For the effect of NCpt dosage on MEB adsorption (Fig. 2a), the results show that the removal efficiency of MEB increased from 75% to 87% by increasing the dose from 0.01 to 0.07 g/L. This is explained by the extra NCpt particles, increased total surface area and improved availability of active adsorption sites, which enable more efficient collisions between the adsorbent and the adsorbate. However, when the dosage rose from 0.07 to 0.13 g, a significant drop in removal effectiveness was seen (from 87% to 5%). Particle aggregation and the (screen effect) [26], which occurs when high adsorbent particle concentrations cause active sites to overlap, are probably to blame for this peculiar decline. Additionally, at such large doses [27], MEB molecules may not be able to reach the NCpt's interior pores due to increased solution turbidity or particle-to-particle interactions [28]. On the other hand, as the dose increased from 0.01 to 0.13 g/L, the adsorption capacity (q_e) decreased from 29.4 to 0 mgg^{-1}. This behavior is explained by the unsaturation of active sites during the adsorption process; the amount of adsorbate available per unit mass of NCpt falls as the mass of the adsorbent increases while the C_o of

MEB stays constant, resulting in a decrease in the concentration gradient. For TC (Fig. 2b), the removal efficiency increased with increasing doses from 0.01 to 0.13 g, and it increased gradually from 47.3% to 84.6%. This consistent increase implies that the saturation of the system is slower for TC, requiring a larger amount of NCpt to reach the maximum efficiency (Sonmez et al., 2022) (Mostafapour et al., 2022). The adsorption capacity decreased from 35.2 to 5.2 mg/g, meanwhile, with the increase in dosage from 0.01 to 0.13 g. This behavior has been attributed to the overlapping of adsorption sites at higher adsorbent concentrations and the dilution of the adsorbate molecules over a larger number of active sites, which leads to a lower effective utilization of the total capacity of the adsorbent (Sahoo and Prelot, 2020).

3.1.4 Effect of C_o

The findings of the MEB removal experiment, as shown in Figure (3a), show that the NCpt and the drug molecules have a strong affinity. The elimination efficiency reached a perfect condition of 100% at lower concentration levels (3 to 30 mg L^{-1}). This suggests that full sequestration from the solution was possible since there were a lot more empty active sites on the NCpt than MEB molecules. The elimination efficiency gradually decreased to 10% at 200 mg L^{-1} when the concentration rose above 40 mg L^{-1}. The saturation of the adsorbent's active sites is the main cause of this tendency. The ratio of adsorbate molecules to accessible surface area rises above the material's capacity with greater loading, where the fixed amount of NCpt becomes the limiting factor. When C_o increased from 3 mgL^{-1} to 70 mgL^{-1}, the adsorption capacity (q_e) consistently increased from 4.3 to 80.9 mgg^{-1}. At larger C_o, the concentration gradient (driving force) "pushes" MEB molecules into the NCpt's framework, causing this amplification. Because it establishes the driving force for mass transfer between the solution and the adsorbent, C_o has a considerable effect on the adsorption process. It's interesting to notice that at the highest C_o (200 mgL^{-1}), q_e decreased to 11.1 mgg^{-1}. This effect, also known as electrostatic hindrance or adsorbate-adsorbate repulsion, occurs when the high density of adsorbed MEB molecules forms a repulsive barrier against incoming ions in addition to possible pore obstruction that restricts access to the internal structure.

When it comes to TC (Fig. 3b), the elimination efficiency was 27.3% at 14 mgL^{-1}. The elimination efficiency showed a steady decrease from 23% to 5.5% as C_o was increased from 46 to 200 mgL^{-1}. This pattern suggests that there are few distinct active sites for TC molecules on the NCpt surface. Due to the adsorbent's limited capacity, these sites quickly get saturated as C_o rises, leaving the majority of the TC molecules in the solution. On the other hand, as C_o increased from 14 to 63 mgL^{-1}, q_e gradually increased from 7.6 to 19.1 mgg^{-1}. This rise is explained by the concentration gradient's improvement, which serves as a catalyst to promote TC molecules' diffusion toward the adsorbent surface. The adsorption capacity of TC onto NCpt remained mostly unchanged when C_o was increased to 200 mgL^{-1}, followed by an equilibrium phase. However, the quick decline in removal efficiency and the comparatively low maximum q_e when compared to MEB indicate that TC molecules face substantial steric hindrance,

most likely as a result of their larger molecular size and complex structure. This obstacle prevents them from penetrating deeply into the NCpt pores, resulting in a surface-dominated adsorption mechanism that rapidly saturates at larger concentrations. At greater TC concentrations, no desorption has been seen, indicating greater stability than MEB.

3.1.5 Impact of contact time

In adsorption research, contact time is a crucial factor as it indicates how long it takes to reach equilibrium and offers crucial information on the kinetics and underlying mechanics of the process. It is essential to comprehend the temporal behavior of adsorption to optimize industrial and environmental applications [29]. As illustrated in Fig. (4a), MEB adsorption onto NCpt demonstrated a two-phase mechanism [30]. In the first stage, a significant percentage of MEB molecules were removed in the initial five minutes of contact due to an incredibly quick adsorption. The strong affinity between the MEB molecules and the adsorbent as well as the abundance of vacant active sites on the NCpt's external surface provide the reason for this rapid phase. After that, as these sites filled up gradually (5–15 min), the rate slowed down and reached equilibrium in just 30 minutes. The quick achievement of equilibrium indicates that surface adsorption is primarily controlling the process, and that MEB's molecular size provides effective access to the NCpt framework with little diffusion resistance. After 30 minutes, the stability of q_e shows that the adsorption and desorption rates have reached equilibrium, indicating full saturation of the available functional sites for both concentrations.

Concerning the adsorption behavior of TC (Fig. 4b), the adsorption capacity increased gradually over time. After 300 min of constant contact, TC reached its equilibrium condition. It appears that TC molecules face significant mass transfer resistance since it takes three hours to achieve equilibrium. Tetracycline's structural complexity and comparatively high molecule size, which cause steric hindrance, may be the cause of this phenomenon [31]. The molecules first occupy the most accessible surface locations, but as the process progresses, intra-particle diffusion (IPD) becomes the rate-limiting phase, requiring TC molecules to gradually move within the NCpt's interior pore structure. The gradual approach to equilibrium suggests that the adsorbent's saturation is a time-dependent process controlled by the bulky TC molecules' sluggish diffusion until the maximum practical capacity is attained at 240 minutes.

It is worth noting that increasing C_o of both drugs didn’t alter the kinetic profile suggesting that the initial concentration has no significant impact on adsorption kinetics of MEB@NCpt or TC@NCpt.

3.2 Isotherm Analysis

The adsorption isotherm defines the fundamental relationship between the equilibrium conc. of the adsorbate in the liquid phase and its corresponding accumulation on the adsorbent surface at a constant temperature. Adsorption equilibrium is established when the solute molecules remain in contact with the adsorbent active sites for a sufficient contact time under dynamic agitation, achieving a steady-state mass transfer. To understand TC-NCpt and MEB-NCpt interactions, eleven multi-parameter

isotherm equations (comprising two, three, four, and five parameters) were methodically employed to fit the experimental data for the sequestration of MEB and TC onto the NCpt. These models included Freundlich, Langmuir, Dubinin-Radushkevich, Temkin, Langmuir-Freundlich, Sips, Toth, Baudu, Fritz-Schlünder, Redlich-Peterson, and Kahn models. The validation of the most reliable isotherm model was conducted by assessing the magnitude of the determination coefficient (R^2) and, crucially, evaluating the physical feasibility of the derived theoretical maximum adsorption capacity (q_{max}) in relation to the empirical experimental uptake. A summary of the determined isotherm parameters is provided in Table 1, and their graphical representation is illustrated in Fig. 5.

The obtained results indicate that the multi-parameter models are characterized by a much better mathematical accuracy in describing the MEB experimental data than the classical two-parameter models. The highest statistical correlations were achieved by the three-parameter Toth (R^2 = 0.971) and Redlich-Peterson (R^2 = 0.971) models, closely followed by Langmuir-Freundlich (R^2 = 0.969), the four-parameter Baudu (R^2 = 0.968), and Sips (R^2 = 0.968) models. Moreover, the classical Freundlich model also showed a good correlation (R^2 = 0.960), which strongly indicates that the uptake of MEB occurs on a highly energetic heterogeneous surface characterized by multi-layer distribution. In contrast, the high statistical correlation coefficients were obtained by the Kahn and Fritz-Schlünder models (R^2 = 0.971 and 0.960, respectively), while their calculated capacities were 223.9 mgg^{-1} and 116.73 mgg^{-1}, respectively, suggesting that both models overestimated the experimental data, it is appropriate to exclude these two models from the interpretation of modeling. Also, because their coefficients of determination were equal to zero (R^2 = 0), the Langmuir, Dubinin-Radushkevich, and Temkin models were unable to adequately describe the adsorption of MEB@NCpt. In particular, the Langmuir model was less successful than the others. Redlich-Peterson and Toth models are especially notable for their outstanding performance and great fitness. The success of these frameworks supports the mixed-mechanism hypothesis because they were expressly created to mimic adsorption on extremely diverse landscapes and to close the mathematical gap between the Freundlich and Langmuir behaviors. This shows that the cationic MEB molecules interact dynamically with a multi-disperse spectrum of active zeolitic sites with different adsorption energy levels, which is in clear agreement with the adsorption kinetics and time-dependent investigations.

In the case of TC adsorption process (Fig. 5b), Langmuir-Freundlich model describes a hybrid adsorption mechanism where the system transitions from Freundlich-like behavior at lower concentrations to a Langmuir monolayer saturation at higher adsorbate concentrations. The excellent fit (R^2 = 0.966) is heavily supported by the calculated q_{max} value of 21.19 mgg^{-1}, which demonstrates an extraordinary convergence with the experimental capacity (q_{exp} = 22.1 mgg^{-1}). This remarkable agreement mathematically validates the L-F model's capacity to simulate how TC molecules initially distribute themselves randomly over the non-uniform active sites of the nano-zeolite before establishing steady-state saturation within the 285 nm particle network. Moreover, Sips model is a mathematical modification of the Freundlich equation designed to eliminate the limitation of continuous, infinite adsorption capacity at high concentrations. Reflecting the same high predictive power as the L-F model,

the Sips model yielded a predicted q_{max} of 21.19 mgg^{-1}, showing a near-perfect consensus with the actual q_{exp} of 22.1 mgg^{-1} in addition to high value of R^2 (0.955). Crucially, the heterogeneity parameter 1/n was found to be significantly greater than unity (3.39). This deviation from 1.0 strongly confirms a highly pronounced surface heterogeneity, where the adsorption energy changes as a function of surface coverage due to localized electrostatic interactions. Both Redlich-Peterson (R-P) and Toth models yielded identical correlation coefficients (R^2 = 0.921). The Toth model is specifically structured to modify the Langmuir equation to better fit sub-monolayer adsorption on highly heterogeneous solid surfaces. The fact that the Toth exponent (n = 1.25) and the R-P exponent (beta = 1.25) deviate markedly from unity (1.0) mathematically underscores that the system cannot be treated as an ideal, uniform monolayer system. Both models, however, offered respectable statistical fits, but they don't have the precise mathematical parameters needed to accurately represent the nano-composite system's structural complexity or offer capacity-related physical inconsistencies. Despite producing a correlation that is mathematically acceptable (R^2 = 0.915), the Kahn model has a significant physical contradiction that makes it unsuitable for this system. The maximum adsorption capacity is significantly overestimated by the model, resulting in an exaggerated value of 53.76 mgg^{-1}, which is more than twice the actual experimental value (q_{exp} = 22.1 mgg^{-1}). The reason for this overestimation is that the Kahn model tends to fail when dealing with adsorbates like TC that undergo localized electronic transitions (zwitterions) during the adsorption process since it is extremely sensitive to the curvature of equilibrium data. Hence, despite its fair R^2, its parameter values are physically unrealistic and rejected. Because the Dubinin-Radushkevich (D-R) model does not represent a homogenous surface or a constant adsorption potential, it is highly regarded in environmental chemistry. Despite having a worse fit (R^2 = 0.911) than the three- and four-parameter models, it is nevertheless able to calculate a very reasonable capacity (24.81 mgg^{-1}), which is quite close to the empirical 22.1 mgg^{-1}. Importantly, the mean free energy of adsorption per molecule of adsorbate (E), which aids in differentiating between physical and chemical adsorption forces, may be calculated using the K_{ad} value. The fit from the traditional Freundlich model was not ideal (R^2 = 0.850). Although the figure of $1/n_F$ = 0.229 (where $1/n_F < 1$ denotes a normal and beneficial adsorption process) accurately suggests surface heterogeneity, it is still a theoretically limited two-parameter equation. The Fritz-Schlünder model is a five-parameter equation that is quite complicated. Ironically, it produced a relatively poor statistical fit (R^2 = 0.773) even though it had the most changeable parameters and predicted a capacity that was quite near to the experimental data (22.00 mgg^{-1}). This phenomenon is a classic example of over-parameterization in mathematics that has no physical significance. It demonstrates that if the fundamental assumptions of the model do not align with the actual chemistry of the adsorbate, merely adding more empirical parameters to an equation does not provide an accurate description of the environmental system. Temkin model makes the explicit assumption that interactions between the adsorbate and the adsorbent are the only reason why the heat of adsorption of all molecules in the layer drops linearly rather than logarithmically with coverage. The low correlation (R^2 = 0.728) suggests that the linear decrease assumption is essentially false for TC. Rather than uniform, continuous interaction decay, the interactions controlling TC uptake are controlled

by pore-filling mechanisms and localized electrostatic attractions (as covered in the Zeta Potential section). A total statistical and structural failure was shown by the determination coefficient of $R^2 = 0$ that the standard Langmuir model produced. This zero value is very instructive and provides conclusive evidence of the nature of the system from the standpoint of physical chemistry. Tetracycline is a bulky, multifunctional molecule with multiple ionizable groups (pKa 3.3, 7.7, 9.7). As a result, its orientation on the negative surface of the NCpt (-13.5 mV) changes continuously with surface loading, creating significant lateral interactions that violate every fundamental assumption of the Langmuir model. Hence, it completely rejects the hypothesis that the adsorption of TC occurs on a thermodynamically homogeneous surface. Moreover, it refutes the formation of an ideal monolayer. The determined $q_{mb} = 17.42\ mgg^{-1}$ is an underestimated figure, despite the fact that the Baudu model had the greatest correlation coefficient ($R^2 = 0.975$) of the eleven investigated models. In conclusion, the mathematical modeling explicitly establishes that multi-parameter models incorporating heterogeneity factors—specifically Langmuir-Freundlich, and Sips models—are the only reliable frameworks for describing TC adsorption onto NCpt. The multi-parameter approach successfully converged with the empirical data, where the Sips and L-F models predicted a capacity close to the experimental capacity. Consequently, the surface of NCpt must be interpreted as an energetically non-uniform landscape with a multi-disperse pore network capable of capturing TC via dynamic, multi-modal pathways.

Table 1
The adsorption isotherm models and their parameters for the adsorption of TC and MEB onto NCpt

Adsorption models		Expression	Parameter	TC	MEB
Two parameters isotherm	Langmuir	$q_e = q_{max}\frac{K_L C_e}{1+k_2 c}$	q_{max} (mgg^{-1})	27.99	79.99
			K_L (L mg^{-1})	0.021	0.12
			R^2	0	0
	Freundlich	$q_e = K_f C_e^{1/n_f}$	K_f (L mg^{-1})	7.41	63.15
			$1/n_F$	0.229	0.087
			R^2	0.85	0.96
	Dubinin-Radushkevich	$q_e = q_{max}\exp(-k_{ad}\epsilon^2)$	q_{max} (mgg^{-1})	24.81	90
		$\epsilon = RTln\left[1+\frac{1}{C_e}\right]$	K_{ad} (mol^2/kJ^2)	0.0021	0.00003
			R^2	0.911	0
	Temkin		b_T (kJ mol^{-1})	509.3	47
			A_T (L g^{-1})	0.894	0.7
			R^2	0.728	0
Three parameters isotherm	Redlich-Peterson	$q_e = \frac{k_R C_e}{1+a_R C_e^{\beta}}$	K_R (L g^{-1})	1.042	50.72
			a_R (L mg^{-1})	0.011	0.26
			B	1.25	1.33
			R^2	0.921	0.971
	Sips	$q_e = \frac{q_{max} K_s C_e^{ns}}{1+K_s C_e^{ns}}$	q_{ms} (mgg^{-1})	21.19	76.81
			K_s (L mg^{-1})	0.0002	0.302
			1/n	3.39	3.69

Adsorption models		Expression	Parameter	TC	MEB
			R^2	0.955	0.968
	Langmuir-Freundlich	$q_e = \frac{q_{max}(K_{LF}C_e)^{MLF}}{1+(K_{LF}C_e)^{MLF}}$	q_{MLF} (mgg^{-1})	21.19	76.9
			K_{LF} (L mg^{-1})	0.083	0.723
			M_{LF}	3.39	3.69
			R^2	0.966	0.969
	Toth	$q_e = \frac{K_T C_e}{(a_T + C_e^{\,Z})^{1/Z}}$	K_T (L mg^{-1})	1.31	67.702
			a_T (L mg^{-1})	0.011	0.262
			Z	1.25	1.33
			R^2	0.921	0.971
	Kahn	$q_e = (q_m b_k c_e)/ (1 + b_k c_e)^{ak}$	q_{mk} (mgg^{-1})	53.76	223.9
			b_K	0.022	0.27
			a_K	1.42	1.578
			R^2	0.915	0.971
Four-parameters isotherm	Baudu	$q_e = \frac{q_m b_o C_e^{1+x+y}}{1+b_o C_e^{1+x}}$	q_{mb} (mgg^{-1})	17.42	76.81
			b_0	2.3E-07	0.302
			X	0.044	0
			Y	5.39	2.698
			R^2	0.975	0.968
Five-parameters isotherm	Fritz Schlünder	$q_e = \frac{q_{max} K_2 C_e^{m2}}{1+K_1 C_e^{m1}}$	q_{mFSS} (mgg^{-1})	22.00	116.73
			K_1 (L mg^{-1})	0.545	0.7258
			K_2 (L mg^{-1})	0.7	0.3441

Adsorption models	Expression	Parameter	TC	MEB
		m_1	0.35	0.1023
		m_2	0.2	0.0595
		R^2	0.773	0.960

3.3 Kinetic Modeling

Five kinetic models, including Mixed 1,2-Order (MFSO), Pseudo-First-Order (PFO), and Pseudo-Second Order (PSO), Avrami, and IPD models, were used to investigate the adsorption process and how MEB and TC move from the aqueous phase to the NCpt surface and to identify the rate-controlling phase in the elimination of TC and MEB. The adsorption kinetics of MEB at 20 mg L^{-1} were examined, and the corresponding kinetic profiles are illustrated in Fig. (6a). Table 2 summarizes the computed model parameters. According to statistical analysis, there is a strong association between experimental data and the PFO, PSO, MFSO, and Avrami models. The high correlation coefficient R^2 (0.98) and the near closeness of the computed adsorption capacities (q_{cal} = 43 mgg^{-1}) to the experimental values (q_{exp} = 45 mgg^{-1}), demonstrate this great agreement. Conversely, the IPD model did not adequately describe the kinetic process, as evidenced by a significantly lower R^2 value (0.297) and (q_{cal} = 26 mgg^{-1}), which is a substantial deviation from the experimental data. At C_o 40 mg L^{-1} (Fig. 6b), a similar kinetic behavior was observed; however, PFO, Avrami, MFSO and PSO models fit for the experimental data, yielding promising correlation coefficients (R^2 = 0.97 for all), in addition to the relatively close match between the calculated adsorption capacity (q_{cal} = 58.8 mg g^{-1}) and the experimental value (q_{exp} = 58.61 mgg^{-1}). Both PFO and Avrami models are more accurate than the PFO and MFSO models. On the other side, a low value of R^2 showed that the IPD model couldn't fit or explain the process, which means the IPD does not manipulate the rate of adsorption at this concentration. As shown in Fig. 6(c), the IPD model did not fit the actual results well; its R^2 was significantly lower (0.86), and the q_{cal} values diverged greatly from the experimental data. The analysis was extended to estimate TC adsorption kinetics onto the NCpt surface, presenting a comparative view of the material's functionality. The kinetic models and related parameters for TC are represented in Fig. 6(c) and Table 5, respectively. At a TC concentration of 10 mg L^{-1}, the experimental results were found to be well represented by four kinetic models. The first two models were the MFSO and PSO models, which determined adsorption capacity q_{cal} of 25.18 and 25.5 mgg^{-1}, respectively and high R^2 (0.99). The other two models Avrami and PFO models come in the next, they also determined a significant agreement with R^2 values of 0.969 and a q_{cal} of 22.82 mgg^{-1}, for both models. In the second TC concentration (20 mg L^{-1}), a comparable kinetic pattern was maintained, as shown in Fig. 6d. Both the PSO and MFSO models continued to provide the most accurate representation of the adsorption process under these conditions, with q_{cal} of 24 mgg^{-1} and good correlation coefficients (R^2 = 0.95). Then, the Avrami and PFO models displayed slightly poor fits with R^2 values of 0.89 and a q_{cal} of 26.17 mgg^{-1}. In contrast, the IPD model's (R^2 = 0.69) is significantly low, indicating a poor match. Even

at this high concentration, the substantial discrepancy between the q_{cal} values and the experimental data further shows that IPD is not the main rate-determining mechanism. The adsorption process may follow a dual mechanism involving a synergy between physisorption and chemisorption, as suggested by the strong similarity between the PSO and MFSO kinetic models with the experimental data [32].

Table 2
The Isothermal models of kinetics and their parameters for the adsorption of MEB and TC onto NCpt

Model	Parameters	TC (Conc., mgL^{-1})		MEB (Conc., mgL^{-1})	
		10	20	20	40
PFO	q_e (mgg^{-1})	22.82	26.17	43.36	58.83
	k_1 (L/mg)	0.058	0.166	0.664	0.884
	R^2	0.969	0.89	0.98	0.97
PSO	q_e (mgg^{-1})	25.35	27.99	43.62	59.67
	k_2 ($gmg^{-1}h^{-1}$)	0.0029	0.0092	0.131	0.063
	R^2	0.99	0.95	0.98	0.97
Mixed 1,2-order Model	q_e (mgg^{-1})	25.18	27.94	43.64	59.66
	K (mgg^{-1} min^{-1})	0.001	0.00009	0.00019	0.0017
	f_2	0.986	0.9965	0.9999	0.9995
	R^2	0.995	0.95	0.98	0.97
Avrami	q_e (mgg^{-1})	22.82	26.17	43.36	58.83
	k_{av} (min^{-1})	0.248	0.419	0.880	0.967
	n_{av}	0.234	0.396	0.755	0.914
	R^2	0.969	0.89	0.98	0.97
IPD	k_{ip} ($mgg^{-1}min^{-1(1/2)}$)	1.455	1.402	2.041	2.623
	c_{ip} (mgg^{-1})	5.44	11.57	26.47	36.025
	R^2	0.86	0.69	0.297	0.32

3.4 Characterization

3.4.1 Chemical bonding

The FT-IR spectra of the synthesized nano-zeolite were analyzed over the range of 400–4000 cm^{-1} to confirm its functional groups and structural framework (Fig. 7). The distinctive vibrational fingerprints observed in the spectrum validate the successful synthesis of the nanomaterial and the preservation of well-structured aluminosilicate frameworks. The sharp constant absorption band that found at 452.66 cm^{-1} is refers to the internal T–O bending modes T = Si or Al within the fundamental SiO_4 and AlO_4 tetrahedra. While by moving upward we found a sharp and well-defined peak appearing at 783.41 cm^{-1} represents the external symmetric stretching vibrations of the T–O–T linkages. This specific band performs as an essential indicator for the structural probity and successful crystallization of the zeolitic phase. The strongest and most important framework band is be based as a broad envelope at 1007.63 cm^{-1}, which is obviously attributed to the internal asymmetric stretching vibrations of the Si–O–Si and Si–O–Al structural bonds. The position of this primary band at a lower wavenumber region at 1007 cm^{-1} strongly indicates a balanced incorporation of aluminum within the silicate lattice, satisfying the structural requirements of the framework. Interestingly, a sequence of weak mixture and overtone bands attached with the silica lattice vibrations was successfully detected at 1939.17 cm^{-1}, 1987.53 cm^{-1}, and 2070.40 cm^{-1}. These overtones are characteristically enhanced in nanomaterials, where the substantial increase in the external surface area and structural boundaries magnifies these subtle lattice reflections. Furthermore, the presence of localized water molecules and highly active surface functional groups was verified. The distinct band resolved at 1637.03 cm^{-1} is directly ascribed to the H–O–H bending (deformation) vibrations of physically entrapped water molecules. This deformation mode is coupled with the highly intense, broad absorption envelope centered at 3402.52 cm^{-1} representing the fundamental O–H stretching vibrations. This broad peak is indicative of a complex hydrogen-bonding network involving both the zeolitic water confined within the intra-crystalline channels and the active surface silanol groups (Si–OH). Consequently, the collective FT-IR spectral analysis firmly corroborates the successful synthesis of a highly crystalline nano-adsorbent possessing excellent surface reactivity appropriate for subsequent mass-transfer and adsorption operations.

Table 3 reveals the changes in the chemical bonds of NCpt after MEB and TC adsorption

Table 3
A comparison between the diffraction peaks of NCpt with TC@NCpt and MEB@NCpt

Wavenumber (cm^{-1})	Vibrational Mode Assignment	Structural Significance	Wavenumber (cm^{-1})	
			MEB@NCpt	TC@NCpt
452.66	Internal T–O (T = Si, Al) bending	Internal tetrahedral framework deformation	Shifted to 403.1	Shifted to 422.6
718.2& 783.41	Symmetric T–O–T stretching	Inter-tetrahedral linkages/crystalline phase indicator	Shifted to 711.2& 789.5, respectively with less intensity	Shifted to 721.0& 797.1, respectively with less intensity
1007.63	Internal asymmetric Si–O–Si / Si–O–Al stretching	Fundamental aluminosilicate framework backbone	Shifted to 1006.6	Shifted to 1015.7 with less intensity
1637.03	Water deformation (H–O–H bending)	Physically adsorbed zeolitic water molecules	Shifted to 1632.7 with less intensity	Shifted to 1630.3 and became wider with less intensity
1939.17	Framework overtones / combination bands	Characteristically pronounced silica lattice vibrations	Shifted to 1935.6 with less intensity	Shifted to 2000 with less intensity
1986.53	CO-like metal–carbonyl species		Slightly shifted to 1992.8 and less intensity	Shifted to 1996.6 with higher intensity
2070.4	Framework overtones / combination bands	Characteristically pronounced silica lattice vibrations	Shifted to 2058.0	Shifted to 2047.5 with
2145	CO-like metal–carbonyl species			Shifted to 2162 with higher intensity
Around 3400	O–H stretching (hydrogen-bonded)	Associated with silanol (Si–OH) groups and channel water	Less intensity	Shifted to 3426 with less intensity

For the adsorption of TC onto NCpt, all the bands of TC@NCPT showed lower intensity compared to that of NCpt except the two bands at 2162 cm^{-1} and 1987 cm^{-1} (Fig. 7b). This is attributed to that the band at 2162 cm^{-1} corresponds to CO-like metal–carbonyl species, not the aluminosilicate lattice, linearly bound to cationic sites or other extra-framework cations [33] [34]. The increase in this band suggests the occurrence of ion exchange between cations on NCpt and TC species (TC^{+}) or more cations become

available or more molecules bind to CO- onto NCpt. This is results in more adsorbate–cation complexes being formed on the zeolite surface or stabilization of CO-like vibrational modes from adsorbed species, which absorb strongly in this region. Moreover, there are various shifts in the locations of the bands of TC@NCpt compared to NCpt as listed in Table 3. These noticeable changes refer to the interaction between TC and NCpt. The decrease in the intensity of the band around 3400 cm^{-1} suggests the contribution of -OH (hydrogen bonding) in the adsorption of TC onto NCpt. For MBE@NCpt, all the bands of MBE@NCPT showed lower intensity compared to that of NCpt except the peak around 2070.4, it shifted to 2047 with the same intensity. All the other bands have been shifted as listed in Table 3 suggesting an interaction between TC and NCpt with special focus on hydrogen bonding as the bands associated with OH- have been shifted with less intensity.

3.4.2 Mineral analysis

The crystallographic properties of the NCpt sample were examined using X-ray diffraction (XRD) analysis before and after the adsorption of MEB and TC to investigate potential structural modifications. The XRD pattern of the pristine NCpt exhibited characteristic diffraction peaks at 2θ = 9.81°, 11.19°, 17.47°, 22.35°, 26.03°, 28.12°, 31.89°, and 32.70° [35] [36]. These diffraction peaks are in good agreement with the standard reference pattern of clinoptilolite (JCPDS card No. 00-022-1236). Additionally, the Scherrer equation was used to determine the average crystallite size of the pure NCpt based on the widening of the peak at 2θ = 22.35° (FWHM ≈ 0.73°), resulting in a value of roughly 11.1 nm. One important aspect that enhances the adsorbent's surface reactivity is its nanocrystalline structure. However, the presence of other peaks (12.88°, 19.66°, 29.91°, 33.59°, 36.07°, 37.13°, 39.64°, 42.57°, 44.95°, 6.28°, 51.69°, 54.09°, 61.65°, 64.95°, 69.19°, and 71.19°) arises from some impurities in the NCpt such as feldspar, illite, and opal-CT, which consists of nanocrystalline blades of cristobalite and tridymite [37]. Following adsorption, the XRD patterns showed that the NCpt’s characteristic peaks were still present, indicating that the fundamental crystalline structure remained intact. However, a shift in peak positions and a reduction in peak intensity were observed, as detailed in Table 4. The peak shifting can be attributed to molecular interactions between the NCpt framework and the adsorbed pollutants, which may have induced slight structural distortions. Meanwhile, the decrease in peak intensity suggests that TC and MEB were incorporated into the NCpt framework or adsorbed within its pores, partially blocking diffraction from the framework planes, a behavior commonly reported for organic pollutant adsorption on zeolitic materials [38] [39] [40].

Table 4
A comparison between Peaks of NCpt, MEB@NCpt and TC@NCpt

Peak location (°)			**Change**
NCpt	MEB@NCpt	TC@NCpt	
9.81	10.01	9.84	Shifted and decreased in intensity
11.19	11.34	11.16	
12.88	13.21	13.28	
17.47	17.72	17.38	
19.66	19.83	19.77	
22.35	22.54	22.68	
26.03	26.18	26.27	
28.12	28.17	27.98	
29.91	30.18	30.38	
31.89	32.13	32.10	
32.70	32.96	32.89	
33.59	32.03	33.02	
36.07			Disappeared
37.13	37.04	37.13	Shifted for MEB and there is no change for TC
39.64			Disappeared
42.57		43.49	Shifted and decreased in intensity
44.95	44.99	45.08	Shifted and decreased in intensity
46.28			Disappeared
51.69			
54.09			
61.65			
64.95			
69.19			
71.19			

3.4.3 Surface characteristics

The specific surface area and pore volume were calculated using the BET method, which is based on nitrogen adsorption/desorption isotherm measurements at 77 K. The results (Fig. 9) reveal that the NCpt follows a type IV isotherm with an H3 hysteresis loop. According to the IUPAC classification, this is characteristic of mesoporous materials, where capillary condensation occurs within mesopores [41]. The isotherm shows a hysteresis loop during desorption after an initial monolayer-multilayer adsorption area. According to the BET examination, the specific surface area of pristine NCpt was 34.149 m^2/g, with a total pore volume of 0.1624 cm^3/g. Following both TC and MEB adsorption, the specific surface area significantly dropped to 21.046 m^2/g and 17.258 m^2/g, respectively, indicating surface occupation by the adsorbed molecules. However, the pore volume remained relatively unchanged at 0.1653 cm^3/g (TC@NCpt) and 0.1664 cm^3/g (MEB@NCpt), suggesting that adsorption primarily took place on the external surface rather than within the internal pores of the NCpt. This is attributed to the interaction between the drug molecules and the NCpt surface functional groups, which became occupied after adsorption, reducing available surface area. These results are consistent with previous studies on adsorption of organic pollutants on zeolitic materials, where the surface coverage generally reduces the surface area without much change in pore volume when adsorption is mainly at exterior sites [42]. Moreover, the pore size distribution showed an average pore diameter of 16.75 nm for the pure NCpt. This value significantly increased to 20.51 nm for TC@NCpt and 24.08 nm for MEB@NCpt during the adsorption process. A pore-mouth blocking mechanism associated with preferential adsorption within the smaller pores is strongly suggested by this rise in average pore size, the notable decrease in specific surface area, and the nearly constant total pore volume. In particular, the active sites on the exterior surface and at the entrances of the smaller mesopores are strongly interacted with the comparatively big and bulky molecules of TC and MEB. During the BET measurement, these smaller pores are blocked, making them inaccessible to nitrogen molecules. As a result, the device only detects the remaining wider, unoccupied pores, shifting the mathematical average of pore size to a higher value. This demonstrates unequivocally that deep interior diffusion is not the dominant adsorption mechanism as external surface contacts.

3.5 Reusability Study

To evaluate the economic feasibility and sustainability of the NCpt adsorbent, a series of five sequential adsorption–desorption cycles were conducted. Regeneration efficiency was investigated using two independent solvents: green tea extract (GTE) as a green desorbing agent, and ethanol as the traditional solvent. As illustrated in Fig. 10, NCpt showed excellent reusability after adsorption of both TC and MEB over four consecutive cycles. Figure 10 reveals that there is an increment in the adsorption capacity of NCpt after regeneration with GTE. This may refer to the occurrence of distinct chemical activation. Green tea extract is highly enriched with polyphenolic and catechins compounds which contain (–OH) functional groups. During each regeneration cycle, a layer of these functional groups attached to the surface of NCpt via electrostatic interactions and hydrogen bonding. The accumulated (–OH) functional groups onto NCpt act as secondary driving forces, strengthen hydrogen bonding and π-π stacking interactions with the electron-rich aromatic rings of TC molecules. For MEB, the localized negative

charge density developed by the chemisorbed tea polyphenols exponentially boosts the electrostatic attraction toward the cationic form of MEB in the solution. This phenomenon aligns with findings by [43], which suggested that zeolitic frameworks show high affinity towards plant-derived polyphenols, effectively transforming NCpt into a bio-composite. The same trend has been observed in case of ethanol. However, NCpt possess amorphous silica debris and mineral impurities, in addition to tightly bound hydration shells within their microporous cavities. Ethanol is physically purging the NCpt channels and stripping away the deeply entrapped organic impurities. Therefore, facilitating smoother IPD without degrading the crystalline framework [43].

3.6 Comparison with literature

NCpt showed low adsorption capacity toward TC and MEB compared to the literature (Table 5). This may be attributed to that the developed NCpt is natural product and doesn't undergo any modification.

Table 5
A comparison of the maximum adsorption capacities of TC and MEB onto NCpt compared to other adsorbents

Adsorbate	Adsorbent	q_{max} (mg/g) or removal %	Optimum conditions				Citations
			pH	C_o (mg/L)	Time	Adsorbent mass/dose	
TC	Microplastics (MPs)	93.23%	10	10	55	1.25	[44]
	CdTe QDs@ZIF-8@SA microspheres	101.15 mg/g	6	40	120	40 mg	[45]
	Magnetic Chitosan (CS·Fe_3O_4)	211.21 mg/g	7	50	180	0.5 g/L	[46]
	Fe_3O_4 NPs & Clinoptilolite	180.9 mg/g (98.6%)	8	10	40	1.7 g/L	[47]
	Magnetic activated carbon	714.28 mg/g	4	250	240	0.01 g	[48]
	Graphene oxide	223.7 mg/g	4	200	120	0.5 g/L	[49]
	Fe-Al bimetallic oxides	116.6 mg/g	5	80	240	--	[50]
	Iron and manganese oxides loaded biochar	14.24 mg/g	11	20	--	1.0 g/L	[51]
	Zinc oxide	62.5 mg/g	5	300	30	0.5 g	[52]
	H_3PO_4-activated carbon	308.33 mg/g	6.5	-	-	0.6 g	[53]
	SA@MRBC	326.81 mg/g	-	50	10	2 g/L	[54]
	MIL-53@activated carbon sponge hybrid	654.93 mg/g	7	10	180	2 mg	[55]
	Magnetic rice straw biochar	75.60 mg/g (44.4%)	6	25	51	0.83 g/L	[56]
	Co/Zn-ZIFs@pine sawdust	719.0 mg/g	7	-	-	2 mg	[57]

	MOF-199 composite	218.2 mg/g	5–7	-	120	-	[58]
	ZnAl-LDH/bagasse biochar	41.98 mg/g	6	25	120	0.4 g/L	[59]
	NCpt	22.12 mg/g (27.3%)	5	50–200	300	0.01	This work
MEB	Activated carbon	4105 mg/g	5.8	10	-	0.5 g	[60]
	NCpt	80.9 mg/g (100%)	7	5-200	30	0.01	This Work

4 Conclusions

In this study, Nano clinoptilolite (NCpt) was successfully synthesized from natural zeolite as an eco-friendly, highly economic, and sustainable adsorbent tailored for the efficient removal of pharmaceutical contaminants, specifically Mebeverine (MEB) and tetracycline (TC), from aqueous environments. This research directly aligns global sustainability initiatives, contributing toward United Nations SDGs (6, 11 and 14). X-ray diffraction (XRD) investigation verified the preservation of the pure clinoptilolite phase with an estimated nanocrystalline framework size of 11.1 nm. Physicochemical analysis revealed that the adsorption routes, where IPD, pore filling, and electrostatic interactions together determine the removal effectiveness, are strongly influenced by the operational pH, dose and C_o. Regeneration tests further showed the remarkable lifetime and structural integrity of the synthesized NCpt, which maintained excellent performance even after five successive cycles of desorption and adsorption. Importantly, the use of green tea extract (GTE) as a green, bio-based eluent offered a very sustainable and non-toxic substitute for traditional ethanol, highlighting the treatment method's environmental feasibility. In conclusion, the produced NCpt is a durable, and ecologically safe adsorbent that provides a strong and scalable platform for the removal of significant pharmaceutical contaminants from industrial effluent.

Declarations

Ethical Approval

The submitted work is original, and it was not published elsewhere in any form or language.

Consent to Participate

All authors agreed with the content and that all gave explicit consent to submit.

Consent for publication

Not applicable.

Competing interests

No conflict of interest of any type

Funding

The characterization analyses for this research paper were funded by the United States Agency for International Development (USAID). The contents are the responsibility of the Authors and do not necessarily reflect the views of USAID or the United States Government. The direct access funding provided only by The Science, Technology & Innovation Funding Authority (STDF, Egypt) in cooperation with The Egyptian Knowledge Bank (EKB).

Author Contribution

Shorouk Goda is responsible for Writing – original draft, Data curation, Formal analysis and Investigation. Nabila Shehata is responsible for conceptualization, Methodology, Visualization, and Validation. Ahmed Hassan, Tabbi Wilberforce, Nabila Shehata: contributed into Supervision, and Writing – review & editing

Acknowledgement

We have no knowledge except what our GOD have taught us. Indeed, it is him who is the Knowing, the Wise.

Data availability

Data will be made available on request.

References

1. Baba IA, Abdulkareem AS, Tijani JO. Photo-Fenton treatment of emerging pollutants in municipal wastewater using nanocatalysts: A sustainable approach. Results Chem. Feb. 2026;20:102999. 10.1016/J.RECHEM.2025.102999.
2. Shah R, et al. Pharmaceuticals and personal care products: Sources, occurrences, toxicities, and degradation by advanced oxidation and reduction processes- a review. Sep Purif Technol. May 2026;389:135850. 10.1016/j.seppur.2025.135850.
3. Masood AS, Ali MS, Manzar MS, Khan NA, Khan AH. 2 - Current situation of pharmaceutical wastewater around the globe, Khan AH, Khan NA, Naushad M, and H. A. B. T.-T. T. of PAziz W,

editors, Elsevier, 2023, 19–52. doi: https://doi.org/10.1016/B978-0-323-99160-5.00013-8.

4. Tao W, Zheng X, Liu P, Zhang Y, Di B, Qiao H. Occurrence and removal of pharmaceuticals in hospital wastewater and the contribution to wastewater treatment plants. Environ Res. 2025;279:121752. https://doi.org/10.1016/j.envres.2025.121752.
5. Almashaqbeh O, Emmanouil C, Alsalhi L. Quantification of Pharmaceuticals in Sludge Produced from Wastewater Treatment Plants in Jordan and Environmental Risk Assessment. Toxics. 2026;14:62. 10.3390/toxics14010062. no. 1.
6. Gilbody JS, Fletcher CP, Hughes IW, Kidman SP, COMPARISON OF TWO DIFFERENT FORMULATIONS OF MEBEVERINE HYDROCHLORIDE IN IRRITABLE BOWEL SYNDROME. Sep.,, *Int. J. Clin. Pract.*, vol. 54, no. 7, pp. 461–464, 2000, https://doi.org/10.1111/j.1742-1241.2000.tb10900.x
7. Xu L, Zhang H, Xiong P, Zhu Q, Liao C, Jiang G. Occurrence, fate, and risk assessment of typical tetracycline antibiotics in the aquatic environment: A review. Sci Total Environ. 2021;753:141975. https://doi.org/10.1016/j.scitotenv.2020.141975.
8. Qing C. Investigation of tetracycline antibiotic residues in drinking water and its health risk study in He'nan Province. Zhongguo shipin weisheng zazhi. Jun. 2023;35. 10.13590/j.cjfh.2023.06.009.
9. Ozcan F, Celik A, Arserim NB, DETERMINATION OF TETRACYCLINE GROUP ANTIBIOTICS RESIDUES IN THE TIGRIS RIVER AND AGRICULTURAL LANDS FED BY TIGRIS RIVER AND REDUCTION OF UNCONSCIOUS USE., no. 9, pp. 1294–301, 2024.
10. Xu Y-C, Liu G-H, Xu Y-H, Zhao T, Zheng H, Tan X-Y. Physiological and transcriptomic analyses reveal the toxicological mechanism and risk assessment of environmentally-relevant waterborne tetracycline exposure on the gills of tilapia (Oreochromis niloticus). Sci Total Environ. 2022;806:151290. https://doi.org/10.1016/j.scitotenv.2021.151290.
11. Shao S, Wu X. Microbial degradation of tetracycline in the aquatic environment: a review, *Crit. Rev. Biotechnol.*, vol. 40, no. 7, pp. 1010–1018, Oct. 2020, 10.1080/07388551.2020.1805585
12. Xu LS, Wang WZ, Deng JB, Xu WH. The residue of tetracycline antibiotics in soil and Brassica juncea var. gemmifera, and the diversity of soil bacterial community under different livestock manure treatments. Environ Geochem Health. 2023;45(1):7–17. 10.1007/s10653-022-01213-z.
13. Peng A, Wang C, Zhang Z, Jin X, Gu C, Chen Z. Tetracycline photolysis revisited: Overlooked day-night succession of the parent compound and metabolites in natural surface waters and associated ecotoxicity. Water Res. 2022;225:119197. https://doi.org/10.1016/j.watres.2022.119197.
14. Sohel MD, Rahman MS. Environmental contaminants and ecotoxicological consequences of antibiotics and personal care products in freshwater ecosystems: Monitoring and management strategies – A review and meta-analysis. Environ Nanatechnol Monit Manag. Jun. 2026;25:101119. 10.1016/J.ENMM.2025.101119.
15. Kubiak A, Lima S, Li Puma G. Adaptive bioinspired Light Emitting Diode-Internet of Things (LED-IoT) assisted solar packed bed photocatalytic reactor system for naproxen removal from real wastewater matrices, *Chem. Eng. J.*, vol. 522, p. 167518, Oct. 2025, 10.1016/j.cej.2025.167518

16. França DB et al. The versatility of montmorillonite in water remediation using adsorption: Current studies and challenges in drug removal, *J. Environ. Chem. Eng.*, vol. 10, no. 2, p. 107341, 2022, https://doi.org/10.1016/j.jece.2022.107341
17. Thiebault T. Raw and modified clays and clay minerals for the removal of pharmaceutical products from aqueous solutions: State of the art and future perspectives, *Crit. Rev. Environ. Sci. Technol.*, vol. 50, no. 14, pp. 1451–1514, Jul. 2020, 10.1080/10643389.2019.1663065
18. Altintig E, Kabadayi O. Clinoptilolite-Supported ZnO and TiO2 Composites for High-Efficiency Adsorption of Methylene Blue. Processes. 2026;14:575. 10.3390/pr14030575. no. 3.
19. Sayyad FA, Halaghi MM, Shahamat YD. Investigation of lead removal from aqueous solution with nano-composite of Mg-Al layered double hydroxides/EDTA coated on zeolite using central composite design method. Appl Water Sci. 2026;16(5):158. 10.1007/s13201-026-02766-5.
20. Gohary OM. In vitro adsorption of mebeverine hydrochloride onto kaolin and its relationship to pharmacological effects of the drug in vivo. Pharm Acta Helv. Feb. 1997;72(1):11–21. 10.1016/s0031-6865(96)00042-8.
21. Wei F et al. Dec., Insights into the pH-Dependent Adsorption Behavior of Ionic Dyes on Phosphoric Acid-Activated Biochar., *ACS omega*, vol. 7, no. 50, pp. 46288–46302, 2022, 10.1021/acsomega.2c04799
22. Debnath P, Ray SK. Carboxymethyl cellulose grafted and copper nanoparticles filled copolymer nanocomposite for fixed bed adsorption and photocatalytic degradation of antibiotic waste from water. Int J Biol Macromol. 2025;319:145206. https://doi.org/10.1016/j.ijbiomac.2025.145206.
23. Rodríguez-Ramírez CA, Coin F, Vergara-Rubio A, Picón D, Cerveny S, Goyanes S. Enhanced tetracycline removal through 'in situ' europium incorporation in poly (vinyl alcohol) (PVA) electrospun mats: Advantages of this strategy in adsorption and reuse over doping. Chemosphere. 2025;372:144102. https://doi.org/10.1016/j.chemosphere.2025.144102.
24. Qiang Z, Adams C. Potentiometric determination of acid dissociation constants (pKa) for human and veterinary antibiotics. Water Res. Jul. 2004;38(12):2874–90. 10.1016/j.watres.2004.03.017.
25. Ngoc DM, et al. Tetracycline Removal from Water by Adsorption on Hydrochar and Hydrochar-Derived Activated Carbon: Performance, Mechanism, and Cost Calculation. Sustainability. 2023;15:4412. 10.3390/su15054412. no. 5.
26. Elamin NY, Mohamed EA, Elamin MR, Bendary HI, Mubarak MF. Development of alginate-graphene oxide-TiO_2 nanocomposites for highly superior removal of Pb2 + and Cr6 + from wastewater. Int J Biol Macromol. 2026;352:151164. 10.1016/j.ijbiomac.2026.151164. February.
27. Américo-Pinheiro JHP, et al. Adsorptive remediation of naproxen from water using in-house developed hybrid material functionalized with iron oxide. Chemosphere. 2022;289:133222. https://doi.org/10.1016/j.chemosphere.2021.133222.
28. Egbosiuba TC, et al. Biotreatment of clay-based adsorbent to eliminate arsenic (V) ions and malachite green from wastewater: Isotherm, kinetics, thermodynamics, reusability and mechanism. Results Eng. 2024;22:102073. 10.1016/j.rineng.2024.102073.

29. Gohr MS, Abd-Elhamid AI, El-Shanshory AA, Soliman HMA. Adsorption of cationic dyes onto chemically modified activated carbon: Kinetics and thermodynamic study. J Mol Liq. 2022;346:118227. https://doi.org/10.1016/j.molliq.2021.118227.
30. Rodwihok C, et al. Effective removal of hazardous organic contaminant using integrated photocatalytic adsorbents: Ternary zinc oxide/zeolite-coal fly ash/reduced graphene oxide nanocomposites. Colloids Surf Physicochem Eng Asp. Apr. 2023;662:131044. 10.1016/j.colsurfa.2023.131044.
31. Mirizadeh S, Arni S, Elwaheidi M, Salih A, Converti A, Casazza A. Adsorption of Tetracycline and Ciprofloxacin from Aqueous Solution on Raw Date Palm Waste. Chem Eng Technol. Jul. 2023;46:1957–64. 10.1002/ceat.202300193.
32. Kuśmierek K, Fronczyk J, Świątkowski A. Adsorptive Removal of Rhodamine B Dye from Aqueous Solutions Using Mineral Materials as Low-Cost Adsorbents. Water Air Soil Pollut. 2023;234(8):531. 10.1007/s11270-023-06511-5.
33. Kawtharani F, Thomas S, Marie O. In Situ Fourier-Transform Infrared Spectroscopy Study of Carbon Monoxide Adsorption on Silver Nanoparticles Contained in BETA Zeolite Nanocrystals, *Langmuir*, vol. 41, no. 42, pp. 28825–28835, Oct. 2025, 10.1021/acs.langmuir.5c04287
34. D'Ippolito SA, Gutierrez LB, Pieck CL. Optimal Ir/Pt ratio for the ring opening of decalin in zeolite supported catalysts. Appl Catal Gen. 2012;445–6. https://doi.org/10.1016/j.apcata.2012.08.037.
35. Kabuba J, Banza M. Ion-exchange process for the removal of Ni (II) and Co (II) from wastewater using modified clinoptilolite: Modeling by response surface methodology and artificial neural network. Results Eng. 2020;8:100189. https://doi.org/10.1016/j.rineng.2020.100189.
36. Masouleh SY, Mozaffarian M, Dabir B. Landfill leachate treatment using sequential natural zeolite adsorption and peroxymonosulfate activated by UV/Fe2 + system: Effects of main operating parameters and application of fluorescence EEM to monitor organic matters' transformation. J Environ Chem Eng. 2024;12(5):113457. https://doi.org/10.1016/j.jece.2024.113457.
37. Hubner P, Donati N, de Quines LK, Tessaro IC, Marcilio NR. Gelatin-based films containing clinoptilolite-Ag for application as wound dressing. Mater Sci Eng C. 2020;107:110215. https://doi.org/10.1016/j.msec.2019.110215.
38. Ji Y, et al. Efficient and fast adsorption of methylene blue dye onto a nanosheet MFI zeolite. J Solid State Chem. 2021;295:121917. https://doi.org/10.1016/j.jssc.2020.121917.
39. Quan C, Zhou Y, Gao N, Fan X. Unveiling the Superiority: Chlorosulfonic acid–functionalized Y zeolite as an efficient catalyst for lactic acid esterification. Biomass Bioenergy. 2025;200:107993. https://doi.org/10.1016/j.biombioe.2025.107993.
40. Von-Kiti E, et al. Evidence of electronic influence in the adsorption of cationic and zwitterionic dyes on zeolites. Heliyon. Sep. 2023;9(9). 10.1016/j.heliyon.2023.e20049.
41. Sing KSW. The use of gas adsorption for the characterization of porous solids. Colloids Surf. 1989;38(1):113–24. https://doi.org/10.1016/0166-6622(89)80148-9.

42. Muir B, Matusik J, Bajda T. New insights into alkylammonium-functionalized clinoptilolite and Na-P1 zeolite: Structural and textural features. Appl Surf Sci. 2016;361:242–50. https://doi.org/10.1016/j.apsusc.2015.11.116.
43. Margeta KZN, Siljeg M, Farkas A. Natural zeolites in water treatment, *How Eff. is Their Use. Elshorbagy W, Chowdhury R, Ed. Water Treat.*, pp. 81–112, 2013.
44. Zahmatkesh Anbarani M, Najafpoor A, Barikbin B, Bonyadi Z. Adsorption of tetracycline on polyvinyl chloride microplastics in aqueous environments. Sci Rep. 2023;13(1):17989. 10.1038/s41598-023-44288-z.
45. Chen X, et al. Portable fluorescent film and gel microspheres for sensitive multi-color detection and efficient adsorption of tetracycline. Sep Purif Technol. 2025;352:128258. https://doi.org/10.1016/j.seppur.2024.128258.
46. da Silva Bruckmann F, et al. Highly Efficient Adsorption of Tetracycline Using Chitosan-Based Magnetic Adsorbent. Polymers. 2022;14:4854. 10.3390/polym14224854. no. 22.
47. Rouhani M, Ashrafi SD, Taghavi K, Joubani MN, Jaafari J. Evaluation of tetracycline removal by adsorption method using magnetic iron oxide nanoparticles (Fe3O4) and clinoptilolite from aqueous solutions, *J. Mol. Liq.*, vol. 356, Jun. 2022, 10.1016/j.molliq.2022.119040
48. Kargar Samani R, Bazarganipour M, Khamirani MJ, Zilouei H, Ehsani MR. Removal of tetracycline from water using rice straw lignin activated carbon magnetized with $NiFe_2O_4$. Results Chem. 2025;17:102524. https://doi.org/10.1016/j.rechem.2025.102524.
49. Nouri A, et al. Decoration of polylactic acid on graphene oxide for efficient adsorption of methylene blue and tetracycline. Chemosphere. May 2023;322. 10.1016/j.chemosphere.2023.138219.
50. Tang J, et al. Fe-Al bimetallic oxides functionalized-biochar via ball milling for enhanced adsorption of tetracycline in water. Bioresour Technol. Feb. 2023;369. 10.1016/j.biortech.2022.128385.
51. Zhang X, et al. Enhanced adsorption of tetracycline by an iron and manganese oxides loaded biochar: Kinetics, mechanism and column adsorption. Bioresour Technol. Jan. 2021;320:124264. 10.1016/j.biortech.2020.124264. Pt A.
52. Goda MS, Shehata N, Shaltout MH, Zaher A. Emerging Contaminants Removal Using ZnO Nanoparticles: Adsorption of Tetracycline and Ciprofloxacin. ChemistrySelect. May 2025;10:e05432. https://doi.org/10.1002/slct.202405432.
53. Marzbali MH, Esmaieli M, Abolghasemi H, Marzbali MH. Tetracycline adsorption by H3PO4-activated carbon produced from apricot nut shells: A batch study. Process Saf Environ Prot. 2016;102:700–9. https://doi.org/10.1016/j.psep.2016.05.025.
54. Wang L, et al. Magnetic iron-crosslinked sodium alginate modified sugarcane bagasse biochar for rapid and efficient removal of tetracycline hydrochloride in water. Int J Biol Macromol. 2025;330:148099. https://doi.org/10.1016/j.ijbiomac.2025.148099.
55. Kumar N, Kumar V, Garg VK. MIL-53@activated carbon sponge hybrid: A synergistic adsorbent for rapid and efficient tetracycline elimination from aqueous media. Surf Interfaces. 2025;72:107406. https://doi.org/10.1016/j.surfin.2025.107406.

56. Arora B, et al. Bio-fabrication of acid-treated and magnetic biochar from rice straw for tetracycline removal from water: response surface methodology study, reusability, and modelling. Biomass Convers Biorefinery. 2025;15(11):17061–76. 10.1007/s13399-024-06438-9.
57. Zhao Y, et al. Controlled synthesis of bimetallic Co/Zn zeolite imidazolate framework-functionalized pine sawdust for enhanced tetracycline elimination. Colloids Surf Physicochem Eng Asp. 2026;742:140443. 10.1016/j.colsurfa.2026.140443.
58. Lalchhuankima H, Lalzawmliana MG, Saha B, Lalhmunsiama. Synthesis, structural analysis, and tetracycline sequestration efficacy of a novel MOF–clay composite. J Water Process Eng. 2025;80:109101. https://doi.org/10.1016/j.jwpe.2025.109101.
59. Hoang LP, et al. Removal of Tetracycline from aqueous solution using composite adsorbent of ZnAl layered double hydroxide and bagasse biochar. Environ Technol Innov. 2022;28:102914. https://doi.org/10.1016/j.eti.2022.102914.
60. Djebri A, Sadaoui Z, Belmedani M, Domergue L, Trari M. Removal efficiency of pharmaceutical drugs (Mebeverine hydrochloride MEB) by an activated carbon prepared from dates stems. J Environ Health Sci Eng. 2021;19(1):917–31. 10.1007/s40201-021-00658-1.

Scheme 1

Schemes 1 and 2 are available in the Supplementary Files section.

Figures

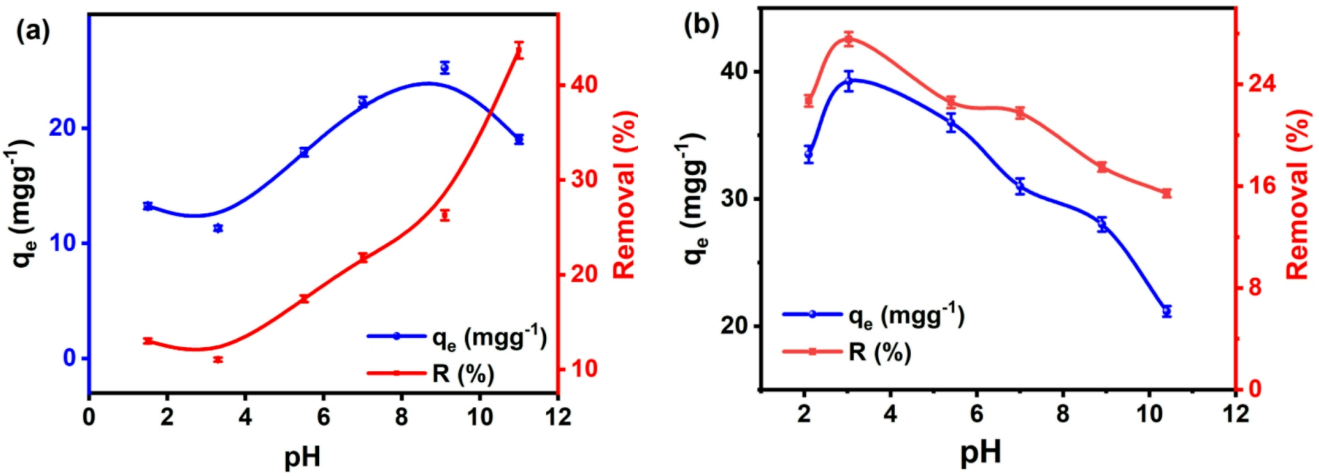

Figure 1

The effect of pH on MEB (a) and TC (b) removal by NCpt at C_o 20 mgL^{-1}, dose 0.01 g, time 12 h and at room temperature

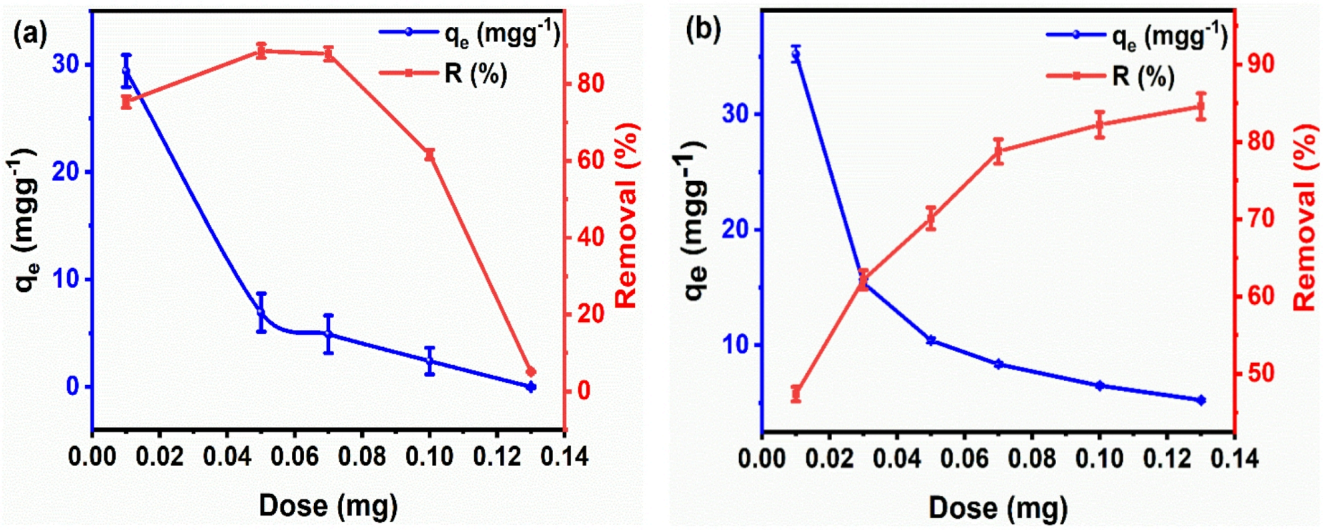

Figure 2

The mass impact on the adsorption capacity and removal of MEB (a) and TC (b) at C_o 20 mgL^{-1}, contact time 7 h, and pH 5 for TC and 7 for MEB at room temperature

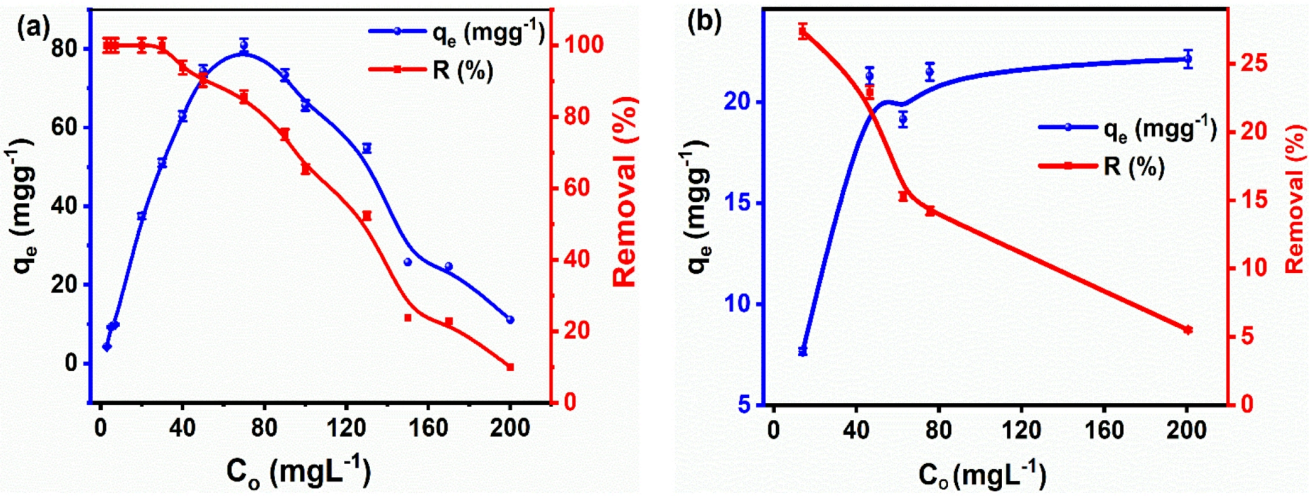

Figure 3

The impact of C_o of MEB (a) and TC (b) on the adsorption of both drug onto NCpt at dose 0.01gL^{-1}, room temperature, and pH 7 and 5, respectively

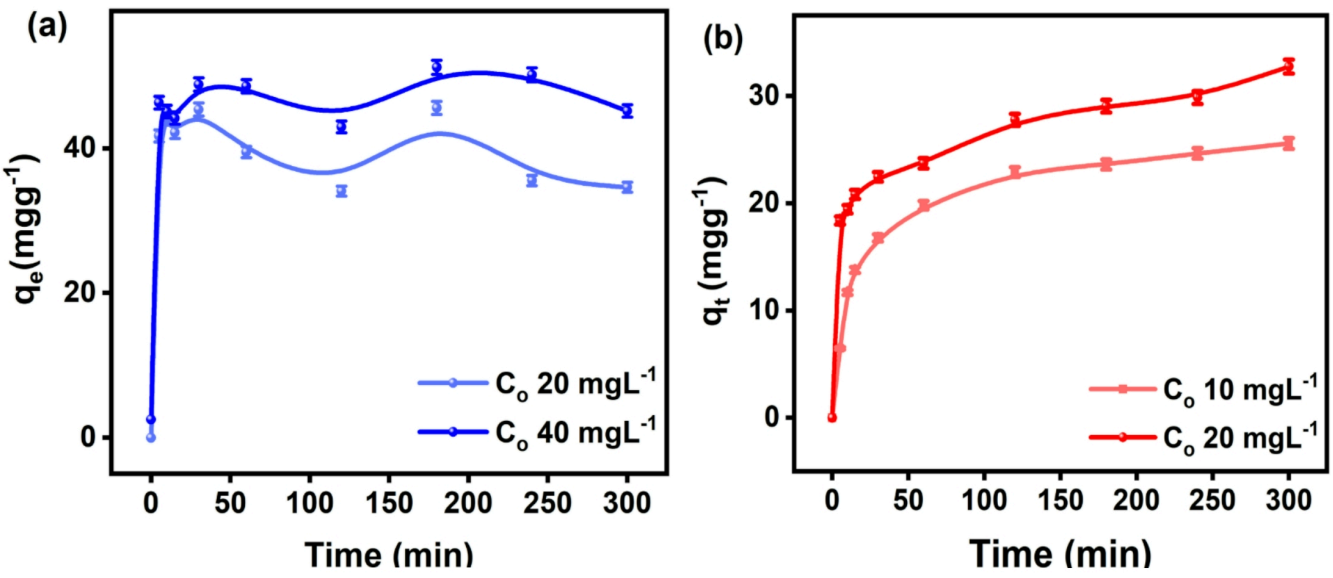

Figure 4

The effect of residence time on the adsorption of MEB onto NCpt at C_o 20& 40 mgL^{-1}, at dose 0.01, pH 7, and at room temperature (a) and TC at C_o 10& 20 mgL^{-1}, dose 0.01, pH 5, and at room temperature (b)

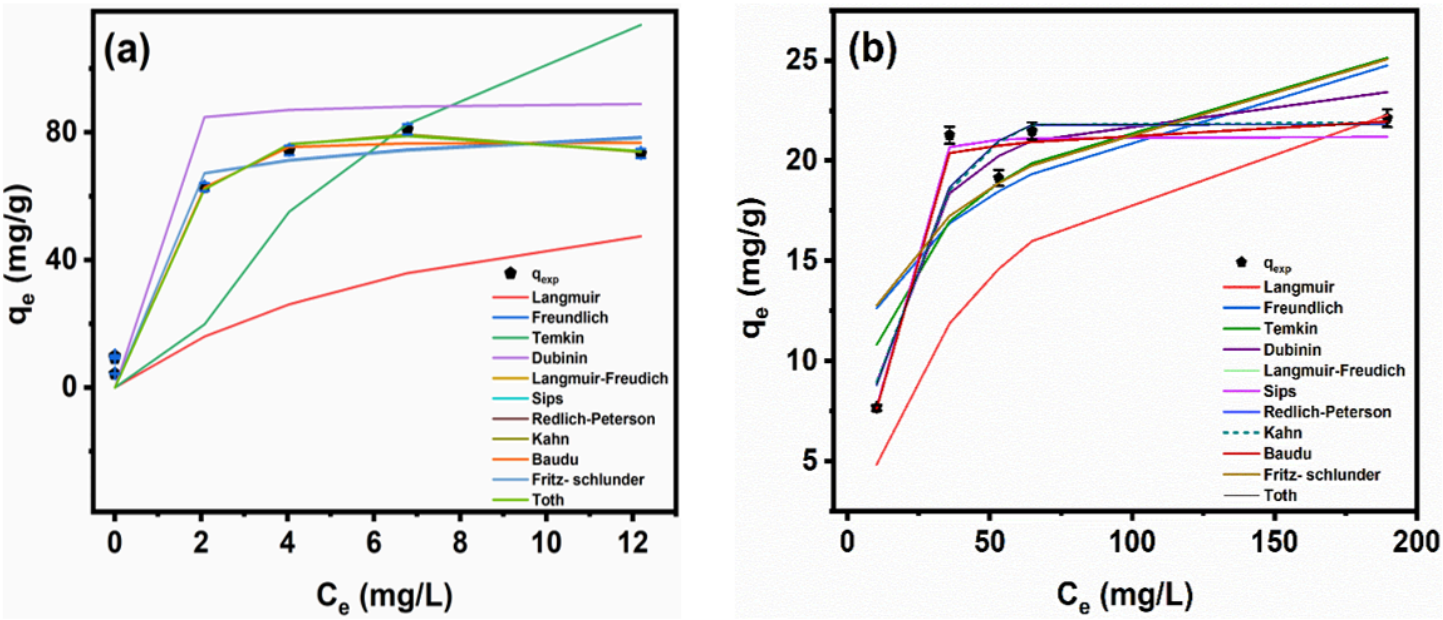

Figure 5

Fitting of adsorption isotherm modelling; Freundlich, Dubinin-Radushkevich, Langmuir-Freundlich, Sips, Redlich-Peterson, Toth, Baudu, khan, Langmuir, Temkin and Fritz-Schlünder for the adsorption of (a) MEB, (b) TC onto NCpt

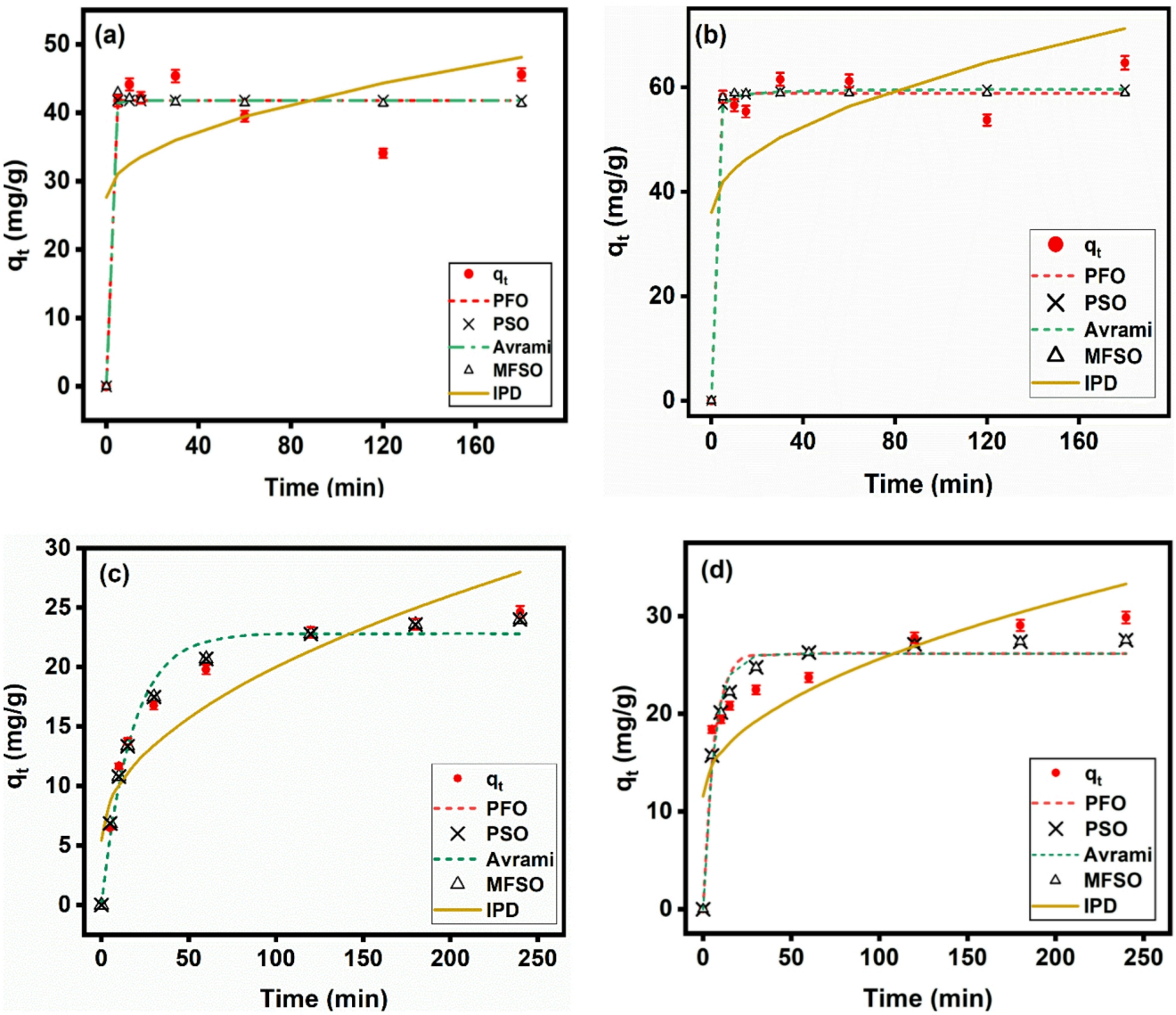

Figure 6

Fitting of PSO, PFO, Avrami, MFSO, and IPD models for MEB adsorption onto NCpt at conc 20 mgL^{-1} (a) and 40 mgL^{-1} (b), and TC adsorption onto NCpt at conc 10 mgL^{-1} (c) and 20 mgL^{-1} (d)

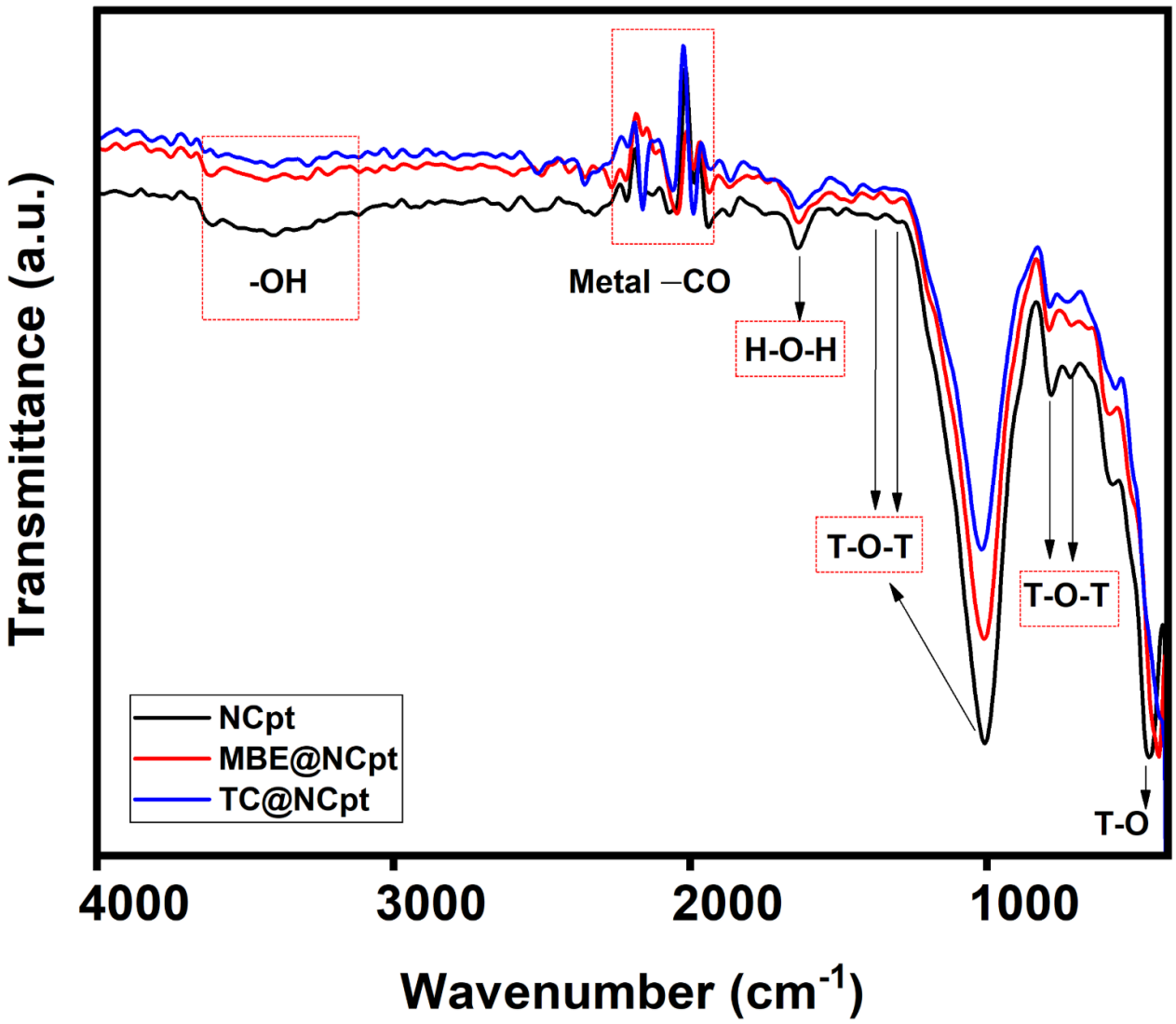

Figure 7

FTIR spectra of NCptpre- and post-adsorption of TC and MEB

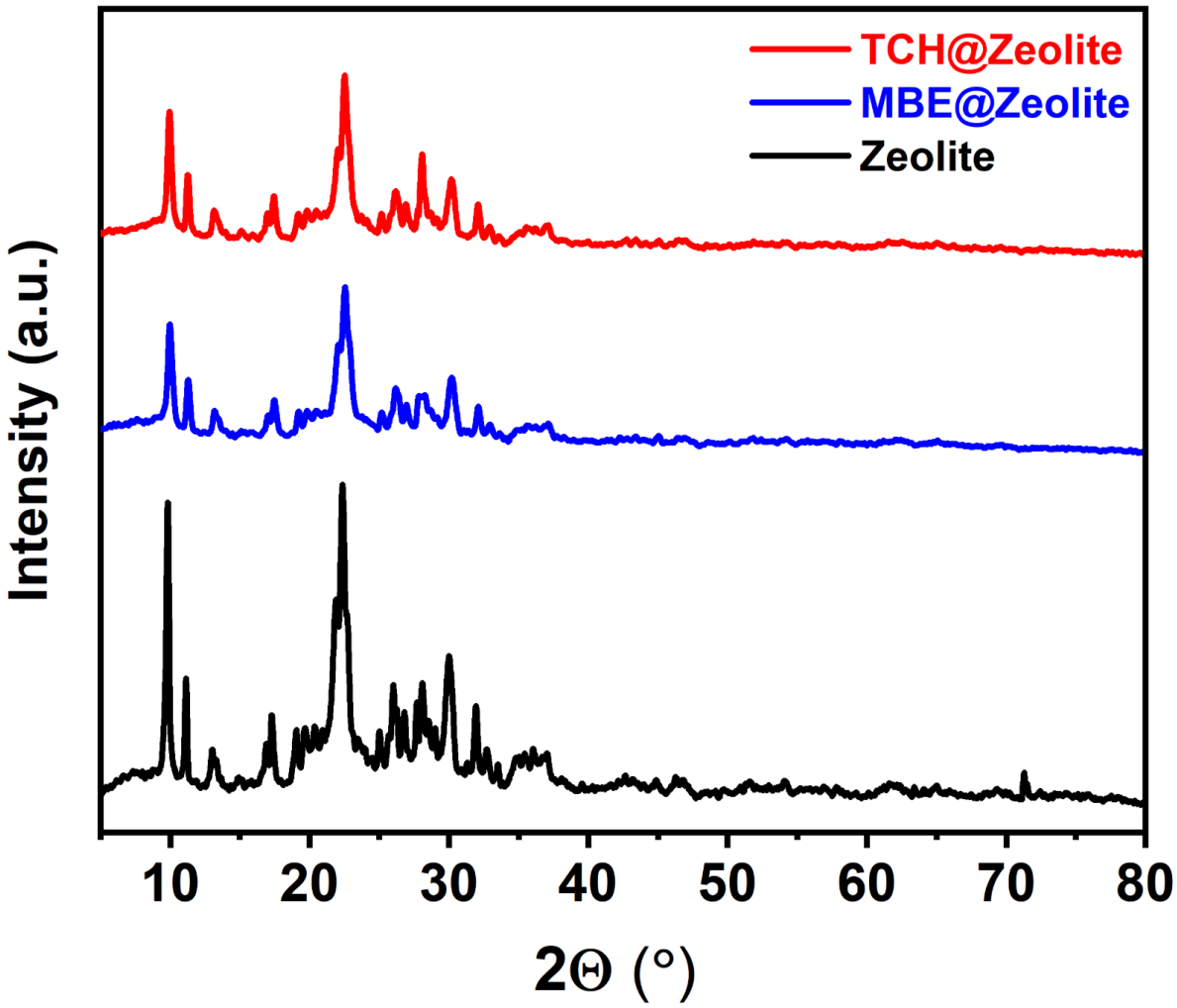

Figure 8

XRD patterns of NCpt, MEB@NCpt and TC@NCpt

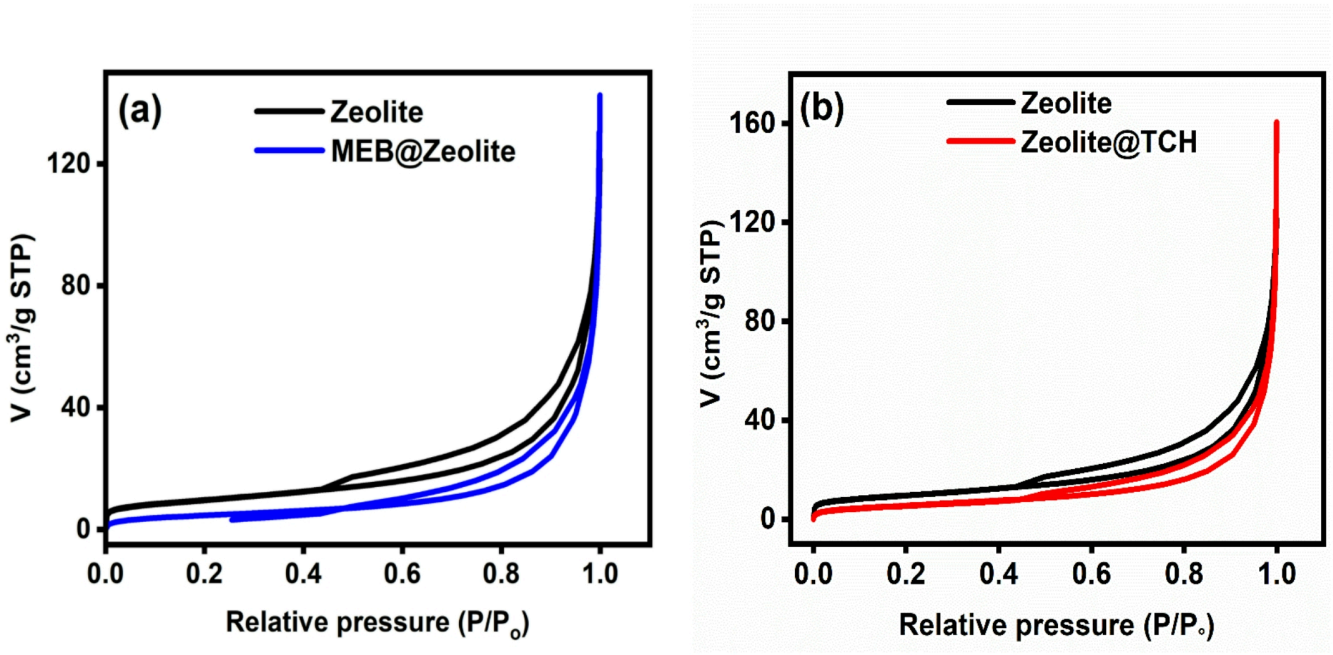

Figure 9

Nitrogen adsorption-desorption isotherms of NCpt and MEB@NCpt (a) and NCpt and TC@NCpt (b)

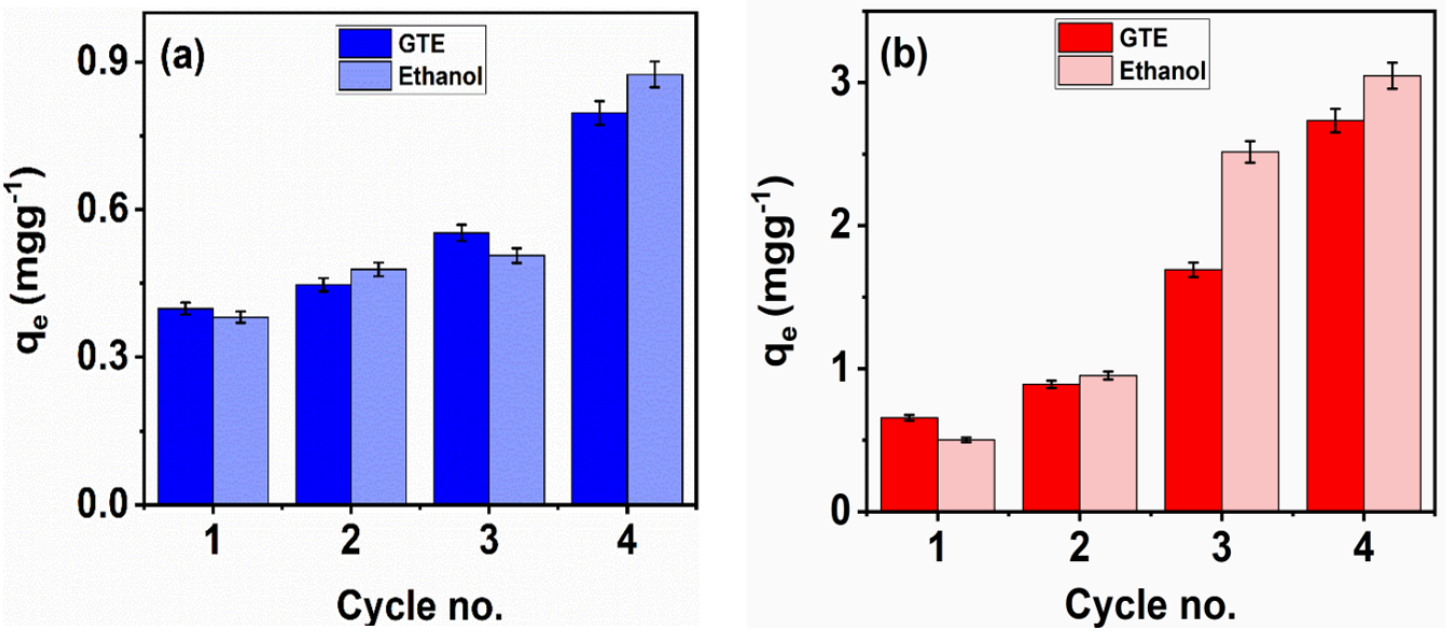

Figure 10

Impact of adsorption/desorption cycles on the adsorption capacity of MEB (a) and TC onto NCpt using GTE and ethanol

Supplementary Files

This is a list of supplementary files associated with this preprint. Click to download.

- scheme1.png
- floatimage1.png